Journal of Materials Chemistry A

ROYAL SOCIETY OF CHEMISTRY

PAPER

View Article Online
View Journal | View Issue

Cite this: J. Mater. Chem. A, 2023, 11, 12080

Bioinspired cone structures with helical micro-grooves for fast liquid transport and efficient fog collection†

Yaxin Guo,‡ Yu-Qiong Luo,‡ Lan Liu, Chenxi Ma, Cuiping Liu, Jingsheng Wang, Xinyu Gao, Xi Yao * and Jie Ju *

A cactus spine with a grooved cone structure provides an ideal model for designs capable of transporting liquids directionally. Inspired by the cactus spine, a lot of artificial liquid transport systems have been reported. In fact, aligned micro-grooves on natural cactus spines are helical rather than straight. Besides, helical structures are frequently found in plant xylem tissue and animal heart tissue, both of which relate closely to liquid transport. Nevertheless, the effect of helical microstructures on liquid transport has not been explored. Herein, we fabricate cones with helical micro-grooves, comparing their liquid transport ability with that of cones with straight micro-grooves. It turns out that the critical volume of a droplet starting to move has decreased from ~0.41 μL to ~0.17 μL and the motion velocity has increased from ~29.72 μm s^{-1} to ~96.73 μm s^{-1}. Helical micro-grooves are speculated to have induced easier conformation transition of droplets from a clam-shell to a barrel state and prolonged the liquid–solid–vapor three phase contact line (TPCL), enlarging the Laplace pressure difference on the droplet and facilitating the droplet's directional motion. By integrating helical grooved cones with highly water-absorbing wood, we construct a fog collection system, demonstrating high efficiency. We envision that this novel helical grooved cone structure will offer new insights for the design of liquid manipulation systems.

Received 28th March 2023
Accepted 11th May 2023

DOI: 10.1039/d3ta01839c

rsc.li/materials-a

Jie Ju received her B.S. degree from Jilin University and Ph.D. degree from the Institute of Chemistry, Chinese Academy of Sciences, under the supervision of Prof. Lei Jiang. She finished her postdoctoral training at Brigham and Women's Hospital, Harvard Medical School with Prof. Ali Khademhosseini and Tufts University with Prof. Brian P. Timko. She is currently a full professor at the School of Materials, Henan University, China. Her research focuses on materials for the water-energy nexus, including zero energy-input fog harvest, solar desalination, liquid super-spreading enabled heat dissipation and electric-energy harvest through manipulating interaction between liquids and surfaces with special wettability.

1. Introduction

Directional liquid transport has been discovered on many natural creature surfaces with unique microstructures, such as the backs of desert beetles with patterned hydrophobic bulges,[1] spider silks with periodic spindle-knots and joints,[2] cactus spines in conical shape and with gradient grooves[3] and *Sarracenia* trichomes with dual-leveled micro-grooves.[4] Inspired by these intriguing structures, various artificial systems capable of propelling liquids directionally have been developed in the past few decades, showing applications in fog-collection,[5–7] underwater bubble manipulating,[8,9] oil/water separation[10–12] and microfluidics.[13,14] In particular, the cactus spine integrates elements facilitating liquid transport—conical shape, gradient of surface free energy, and aligned grooves, making it an ideal model for biomimetic designs capable of driving liquids to move directionally. Taking inspiration from the relationship between microstructures and functions on cactus spines, lots of artificial conical spines have been prepared.[12,15–18] In all these studies, grooved conical spines demonstrate more efficient liquid transport performance compared with non-grooved

Key Lab for Special Functional Materials of Ministry of Education, School of Materials, Henan University, Kaifeng, Henan Province, 475004, China. E-mail: yaoxi@henu.edu.cn; jujie@henu.edu.cn

† Electronic supplementary information (ESI) available. See DOI: https://doi.org/10.1039/d3ta01839c

‡ These authors contributed equally.

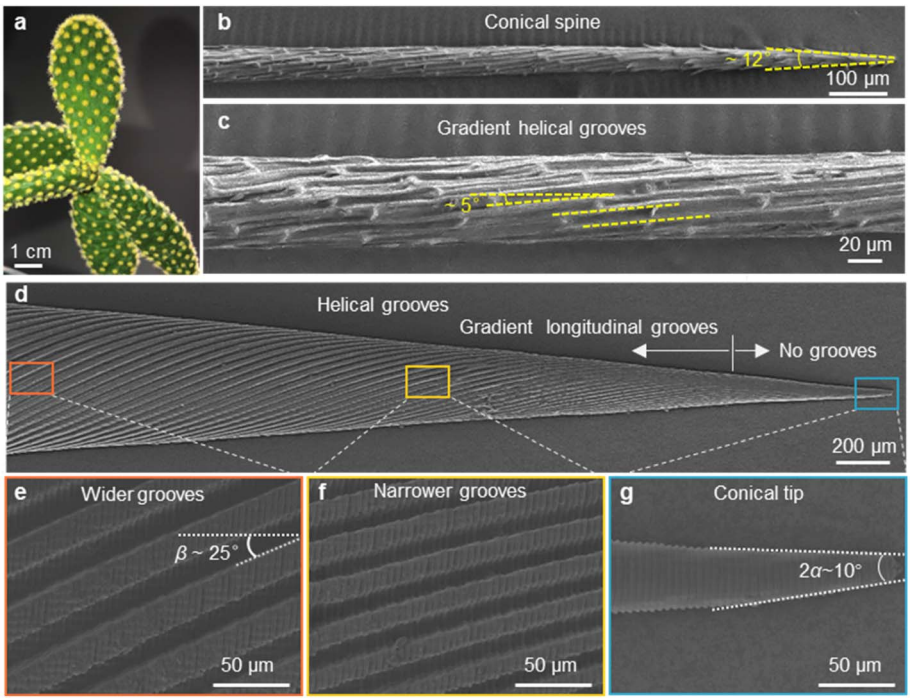

Fig. 1 Appearance and surface structures of natural cactus and artificial helical micro-grooved cones. (a) Optical image of an *Opuntia microdasys* stem covered with clusters of spines and trichomes. (b) SEM image of a single cactus spine. (c) Magnified image of the region near the base of the spine shows gradient helical micro-grooves. The needle-like spine has a conical shape with an apex angle (2α) of ~12.3 ± 1.6° and grooves with a helical angle of ~5.0°. (d) SEM image of an artificial helical micro-grooved cone. Gradient longitudinal micro-grooves are visible on the cone except in the tip region with a length of ~604 μm. (e–g) Magnified images of the base (e), middle (f), and tip (g) of the artificial helical micro-grooved cone. The helical angle β is ~25° (e) and the apex angle 2α is of ~10° (g).

conical spines, *i.e.* a liquid droplet starts to move at a smaller critical volume and at a larger velocity. Such a performance enhancement arises from the enlarged Laplace pressure difference exerted on the two opposite sides of a moving droplet by grooved structures.

Actually, the micro-grooves on natural cactus spines are helical rather than straight. Fig. 1a–c clearly show the aligned micro-grooves with a helical angle of ~5.0°. Interestingly, helical structures are universal in natural creature tissues related to liquid transport. For instance, helical vessels have been found in xylem tissue of various vascular plants to transport water and nutrients from roots to leaves;[19,20] the musculature of the heart is organized in a helical manner, which is beneficial for large ejection fractions.[21,22] Recently, a fibrous helix with alternate hydrophilic–hydrophobic components has been fabricated to separate oil–water mixtures by the liquid guiding effect of a periodic helical structure.[23] Despite the considerable amount of researches that have been performed on the water collection performance of conical-shaped spines, the effect of helical microstructures on liquid transport has not been explored.

Here, we report a conical spine with helical micro-grooves that facilitate efficient fog collection. The water transport behavior on the spines is evaluated from two aspects: motion velocity and critical volume of the droplet that starts to move. The average motion velocity of a droplet on the helical micro-grooved cone is 96.73 μm s^{1}, which is 3 times higher than that on the straight micro-grooved cone (29.72 μm s^{-1}). The helical micro-grooved cone also shows a smaller critical droplet motion volume (0.17 μL) than the straight micro-grooved cone (0.41 μL). It is speculated that the clam-shell conformation and barrel conformation prevail on the straight and helical micro-grooved cones, respectively. Compared with the clam-shell conformation, the barrel conformation produces a liquid–solid–vapor three phase contact line (TPCL) enclosing a larger regional area, inducing greater Laplace pressure force (F_{Laplace}). In addition, the prolonged liquid–solid–vapor TPCL in the helical micro-grooves enlarges the meniscus curvature gradient, further enhancing F_{Laplace}. To demonstrate the superiority of this helical grooved cone on the fog harvest, a fog collection system that couples highly water-absorbing wood at the base of the micro-grooved cone is fabricated. It is anticipated that the principles of helical micro-grooves uncovered in this study will aid in the development of novel designs for continuous and efficient liquid transport systems.

2. Experimental section

2.1. Materials

The cactus (*Opuntia microdasys*) was purchased from the Chinese Academy of Agricultural Sciences, Beijing, China. A single spine was carefully selected and fixed to the sample frame. Sodium chlorite (purity: 80%), acetic acid, 1*H*,1*H*,2*H*,2*H*-perfluorooctyl trichlorosilane, PVA powder (M_w of 89 000–98

000) and DMSO were purchased from Aladdin, Shanghai, China. Polydimethylsiloxane (PDMS, Sylgard 184 Silicone Elastomer Kit) was purchased from Dow Corning. Balsa wood was commercially available.

2.2. Fabrication process of artificial cones

The 3D models of the two types of cones were modeled using Solidworks. Then the cones were fabricated using a 3D printer (nanoArch® S140, Mofa Precision). The resin used in the 3D printing technology is an acrylic photosensitive resin with a curing UV light wavelength of 400 nm. The energy density is 30 mW cm^{-2}, the exposure time is 1 s, the exposure resolution is 10 μm, and the thickness of the printing layer is 10 μm. After 3D printing, the samples were washed with ethanol and then dried. The 3D-printed cone has an apex angle (2α) of ~10°, a length of ~8 mm, a diameter at the base of ~1.5 mm, and depth of the micro-grooves ~50 μm. The width of the micro-grooves decreases gradually from ~40 μm near the base to ~4 μm near the tip (Fig. S1b–i†).

The artificial straight/helical micro-grooved cones were prepared by 3D-printing and three-step replications (as shown in Fig. S1†).

According to Fig. S1a,† the fabrication process involves three steps: PVA replication, PVA shrinkage, and PDMS replication. Initially, a negative PDMS replica was prepared from the 3D printed sample in PVA replication. Then, PVA solution with a mass ratio of PVA : water : DMSO of 20 : 45 : 135 was poured into the negative PDMS replica, degassed at 70 °C, cured at −20 °C for 4 hours, and demolded (Fig. S1j and k†). In PVA shrinkage, the obtained positive PVA replica was soaked in ethanol for 12 hours at room temperature and then freeze-dried to obtain a shrunken PVA cone (Fig. S1l and m†). Subsequently, in PDMS replication, the shrunken PVA cone surface was treated with 1*H*,1*H*,2*H*,2*H*-perfluorooctyl trichlorosilane in an oven at 80 °C for 3 hours (surface fluorination). A negative PDMS replica was then prepared from the shrunken PVA cone. Finally, PDMS solution was poured into the negative PDMS replica, cured, and demolded to obtain shrunken PDMS cones.

The hydrophilic treatment of the cones was performed under oxygen plasma conditions (30 W, 15 s) followed by heating at 65 °C for 10 min. To explore the difference in liquid transport behavior on the straight and helical micro-grooved cones, we maintained the surface wettability of the PDMS cone at a moderate level, with a typical water contact angle of approximately 72° throughout all droplet transport and fog collection experiments.

Due to the inherent accuracy limitation of 3D printing, the length of the groove-free region at the tip of the printed cone is ~1840 μm. To minimize effects from such a region, a typical two-step fabrication composed of PVA replication and PVA shrinkage has been carried out. The shrinkage of the cone structure was accomplished through solvent replacement (water was replaced by ethanol by immersion) of the PVA hydrogel.[24,25] By doing so, the PVA cone contracts isotropically. The proportionally scaled-down cone has an apex angle (2α) of ~10°, a whole length of ~4 mm, a base diameter of ~0.75 mm and length of the groove-free region of ~604 μm (Fig. 1d).

2.3. Delignification process of balsa wood

The delignification solution was prepared by dissolving sodium chlorite in deionized water (1 wt%) and adding acetic acid to adjust the pH value to ~4.6 according to previous research.[26] Balsa wood ($1 \times 1 \times 1$ cm^3) was placed in sodium chlorite at 100 °C for 1–10 hours. The treated wood was washed with deionized water 3 times and freeze-dried.

2.4. Characterization

A field emission scanning electron microscope (SEM) (JSM-7900F, Japan) was used to observe the surface morphology of the samples. Contact angles and droplet motion behaviors were recorded on an optical surface analyzer (LAUDA OSA100, LAUDA Scientific GmbH, Germany). Fourier transform infrared (FT-IR) spectra were obtained on a Frontier IR/FIR STA 8000 thermo-red system (PerkinElmer Inc., USA). The spectra were collected over the range from 4000 to 500 cm^{-1}.

2.5. Droplet transport behavior and observation

An optical surface analyzer (LAUDA OSA100, LAUDA Scientific GmbH, Germany) was used to record the motion of droplets on the cone with a VCR (video cassette recorder) function. The distance between the cone and the mouth of the ultrasonic humidifier was approximately 4.5 cm, and the resulting water vapor was blown vertically to the tip of the cone (see Fig. S2†). To evaluate the critical droplet motion volume precisely, in method 1, a main droplet (0.15 μL) was placed at the cone tip, and additional water was added to the main droplet using a fixed needle at a speed of 10 μL min^{-1}. The main droplet merged with the added droplet and was promoted to move forward (Fig. S3a†). The droplet volume on the cone was calculated using the following equation: $V_{total} = V_0 + V_{addition} = V_0 + \frac{4}{3}\pi({r_1}^3 + {r_2}^3 + \ldots + {r_{end}}^3)$, where V_0 is the main droplet volume of 0.15 μL and $V_{addition}$ is the sum of the droplet volume from the syringe needle before it merges with the main droplet. This was measured using an optical surface analyzer (LAUDA OSA100, LAUDA Scientific GmbH, Germany) with a VCR function, as shown in Fig. S4.† To determine the velocity of droplet motion on the cone, method 2 involved placing the main droplet (0.15 μL) at the top or underneath the cone tip and applying a saturated water vapor flow with a velocity of 40–50 cm s^{-1} to the tip. The condensed water merged with the main droplet and the motion velocity of the main droplet was observed (Fig. S3b†).

2.6. Measurement of the fog collection ability

The straight/helical micro-grooved cone was fixed on the wood (6 hour delignified treatment) horizontally using PVA gel. The droplets transported to the base of the cone could be absorbed by the wood quickly, eliminating the adverse effect on the continuous fog collection and the overall efficiency. A saturated fog flow with a velocity of ~40–50 cm s^{-1}, generated by an ultrasonic humidifier blew vertically to the cone tip. The collected water within 30 minutes was weighed using an

electronic balance with high sensitivity (Sartorius, SQP, SECURA125-1CN) in real.

3. Results

3.1. Appearance and surface structures

The optical image of a natural cactus *Opuntia microdasys* in Fig. 1a illustrates that clusters of spines and trichomes are distributed evenly on the stem. To investigate the spine structure in detail, an individual spine was observed using the SEM. As shown in Fig. 1b and c, the needle-like spine has a conical shape with an apex angle (2α) of $\sim 12.3 \pm 1.6°$. The grooves with a helical angle of $\sim 5.0°$ are micro-grooves and have a gradient in width along the spine, from an average of ~ 6.8 μm near the base to an average of ~ 4.3 μm near the tip. The artificial straight/helical micro-grooved cones were prepared by 3D-printing and three-step replications (as shown in Fig. S1†). Fig. 1d–g show the morphology and structure of the cone with helical micro-grooves. Gradient longitudinal micro-grooves are observed on the cone except at the tip with a length of ~ 604 μm. The magnified SEM images (Fig. 1e and f) show that the width of the micro-grooves gradually decreases from ~ 20 μm near the base to ~ 2 μm near the tip. The helical angle β is 25° and the apex angle (2α) of the tip is $\sim 10°$ (Fig. 1e). Correspondingly, a same-sized cone with straight micro-grooves was also fabricated (Fig. S5†).

3.2. Droplet motion behavior

The water transport behavior on the spines is evaluated from two aspects: critical droplet motion volume and droplet motion velocity. As shown in Fig. 2, with continuous addition of water, the main droplet grows up and moves forward with a specific volume. On the straight micro-grooved cone, the main droplet started to move towards the base of the cone when the volume increased to 0.41 μL (Fig. 2a). In contrast, the critical motion volume of the main droplet on the helical micro-grooved cone is 0.17 μL, which is about 2 times smaller than that on the straight micro-grooved cone (Fig. 2b).

Furthermore, wide field optical microscopy images were captured to estimate the critical droplet motion volume in different regions of the cones. As shown in Fig. S6,† compared with the straight micro-grooved cone, a smaller critical droplet motion volume is observed on the tip, middle and base regions of the helical micro-grooved cone. These results demonstrate that the helical micro-groove facilitates small-sized droplet motion, which is beneficial for water transport.

The motion velocity of the droplet on the two types of cones was investigated under a saturated water vapor flow with an initial droplet (0.15 μL) placed on the top or underneath the cone tip. The straight micro-grooved cone transports the droplet from the tip to the base in 72.67 s with a velocity of 29.72 μm s^{-1}, whereas the helical micro-grooved cone transports the main droplet from the tip to the base in 24.66 s with a velocity of 96.73 μm s^{-1} (Fig. 3a, b and e). Moreover, the droplet adheres to the top side of the straight micro-grooved cone throughout the whole droplet transport process from 0 s to 72.67 s (Fig. 3a),

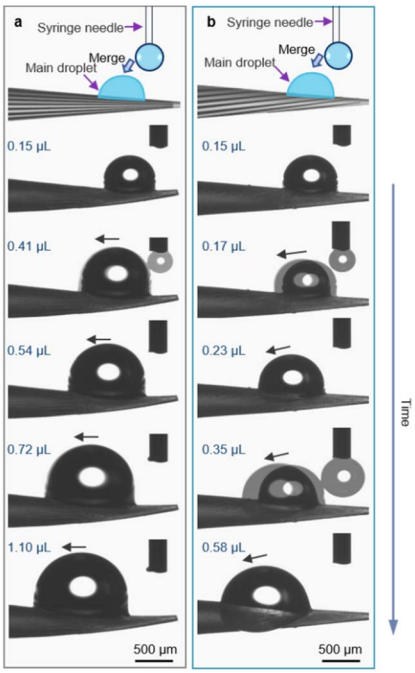

Fig. 2 Optical microscopic observation of the main droplet to determine the critical droplet motion volume on the straight (a) and helical (b) micro-grooved cones. With continuous feeding of water, the main droplet moves from the tip to the base of the cone. The critical droplet motion volume on the helical micro-grooved cone is smaller than that on the straight micro-grooved cone.

whereas the droplet on the helical micro-grooved cone starts to move down at 17.65 s and finally engulfs the helical micro-grooved cone at 24.52 s (Fig. 3b). It has been reported that a droplet on an one-dimensional surface exists in two competing conformations: clam-shell and barrel. Generally, decreasing the liquid contact angle or increasing droplet volume favors the barrel conformation.[27,28]

Although the droplet volume on the helical micro-grooved cone is smaller than that on the straight micro-grooved cone in our case, the clam-shell conformation and barrel conformation prevail on the straight and helical micro-grooved cones, respectively. The helical micro-grooves lead to the transition between the two conformations. From detailed observation of droplet motion on the micro-grooved cones in Fig. S7,† it was found that precursor water films appear in the micro-grooves at the front of the main droplet. The main droplet on the cone moves from the tip to the base along the direction of the micro-grooves. The motion track of the droplet on the straight micro-grooved cone is a straight line, while the motion track of the droplet on the helical micro-grooved cone is a helical line around the cone. It is speculated that this different motion track induces the different droplet conformations on the two types of cones. To eliminate gravity's effect on the droplet's motion track, the transport behavior of another droplet, which was placed initially underneath the cone tip, was evaluated (Fig. 3c–e). In this case, the droplet's motion velocity on the straight and helical

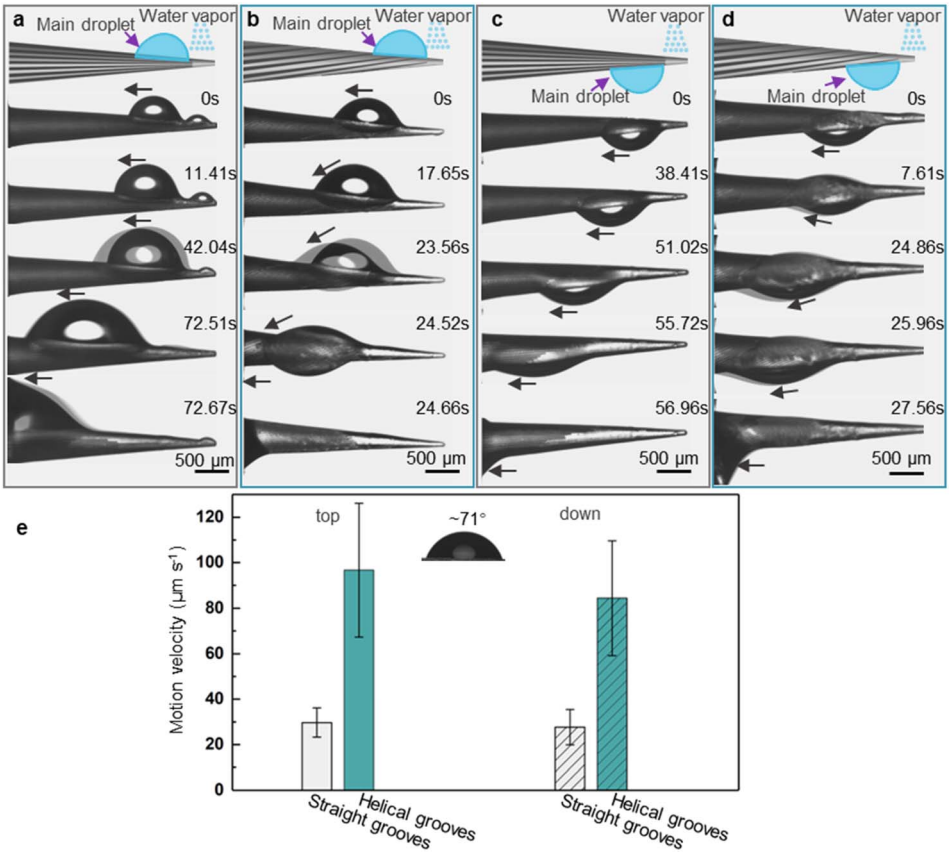

Fig. 3 The droplet's motion behavior on the two types of cones. Snap shots of a typical droplet's motion on the (a and c) straight and (b and d) helical micro-grooved cones. A main droplet (0.15 μL) was placed on the (a and b) top and (c and d) underneath the cone tip. (e) Statistical analysis of the droplet's motion velocity on the two types of cones with different initial positions. Regardless of the initial position, the motion velocity of the droplet on the helical micro-grooved cone is faster than that on the straight one. Moreover, the droplet adheres to one side of the straight micro-grooved cone while engulfing the helical micro-grooved cone during the transport process, that is, clam-shell conformation and barrel conformation prevail on the straight and helical micro-grooved cones, respectively.

micro-grooved cone is 27.70 and 84.39 μm s^{-1}, respectively, close to the situation where the droplet is on top of the cone tip. As for the droplet's conformation evolution over motion along the cones, it shifts to a barrel state on the helical micro-grooved cone through moving upward along the grooves and against gravity at 7.61 s. While on the straight micro-grooved cone surface, the droplet adheres under the cone throughout the whole transport process. Therefore, the clam-shell conformation and barrel conformation prevail on the straight and helical micro-grooved cone, respectively, even in the case where the droplet was placed underneath the cone. The helical angle of the groove of *Opuntia microdasys* is ~5.0°. There is speculation that the cooperation between the force of gravity and the Laplace pressure force exerted on the droplet can be regulated by the helical angle, which can result in different critical droplet motion volumes and velocities.

4. Discussion

It is known that the directional motion of a droplet is controlled by the cooperation of driving and resistant forces, which are due to the Laplace pressure difference $F_{Laplace}$ and solid/liquid interface hysteresis in an asymmetrical cone system. Specifically, water droplets moving along the straight or helical micro-grooved cones experience similar hysteresis resistance. We will therefore not consider it further. $F_{Laplace}$ acting on the droplets in both cases differs much, as detailed in Fig. 4. Generally, grooves supply guidance to droplet motion, inducing motion along the grooves. As in the case of droplet motion on the straight micro-grooved cone, the droplet is prone to adopt clam-shell conformation (Fig. 4a), while on the cone with helical micro-grooves, the droplet transfers to barrel conformation shortly after motion begins (Fig. 4d).

To compare the $F_{Laplace}$ in both cases intuitively, we flatten the curved TPCLs onto planar surfaces. The anamorphic ellipse denoted as ABCD in Fig. 4b and the two arcs denoted as EF–GH in Fig. 4e correspond to the entire TPCL of the droplet in clam-shell conformation on the straight micro-grooved cone and the TPCL at the two opposite sides of the droplet in barrel conformation on the helical micro-grooved cone, respectively. The areas enclosed by the TPCL can be used to roughly indicate $F_{Laplace}$ acting on the droplets.[5,29,30] With the same conicity of 2α,

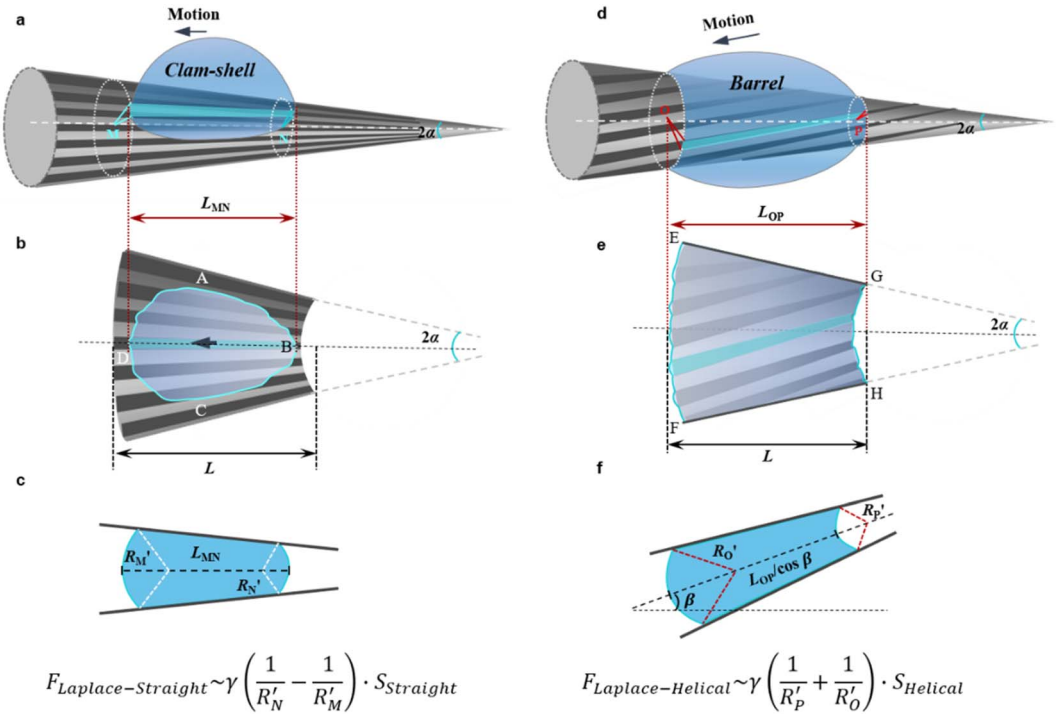

Fig. 4 Estimation of the force induced by the Laplace pressure difference ($F_{Laplace}$) when a droplet is on a cone. The droplet is likely to be in a (a) clam-shell and (d) barrel conformation on the straight and helical micro-grooved cone, respectively. The narrow lake-blue regions in both cases depict the solid/liquid contact regions along the straight or helical groove. The curved TPCL was flattened onto a planar surface, and the areas enclosed by the TPCL ((b) $S_{Straight}$ and (e) $S_{Helical}$) could be used to roughly represent the $F_{Laplace}$ imposing on the droplets. (c and f) Quantitatively, the overall driving force is the sum of the $F_{Laplace}$ along each groove. R'_M, R'_N, R'_O, and R'_P are radii of the local curvatures of contact lines at the two ends of the droplet. L_{MN} and L_{OP} are the lengths of the droplets on the straight and helical micro-grooved cones. $\beta \sim 25°$ is the helix angle of the helical grooves. The local $F_{Laplace}$ induced in both situations scales as: $F_{Laplace-Straight} \sim \gamma\left(\frac{1}{R'_N} - \frac{1}{R'_M}\right)S_{Straight}$ and $F_{Laplace-Helical} \sim \gamma\left(\frac{1}{R'_P} + \frac{1}{R'_O}\right)S_{Helical}$. Since $L_{OP}/\cos\beta > L_{OP} > L_{MN}$, $S_{Helical} > S_{Straight}$; with longer droplets along the longitudinal directional of the helical micro-grooved cone, $R'_P < R'_N$ and $R'_O > R'_M$, $\left(\frac{1}{R'_P} + \frac{1}{R'_O}\right) > \left(\frac{1}{R'_P} - \frac{1}{R'_O}\right) > \left(\frac{1}{R'_N} - \frac{1}{R'_M}\right)$, and therefore $F_{Laplace-Helical} > F_{Laplace-Straight}$.

while $L_{OP} > L_{MN}$, the area of the sector is clearly larger than that of the ellipse.[31] To compare the $F_{Laplace}$ quantitatively, we take out the solid/liquid contact area along one individual groove, the regions in lake-blue in Fig. 4a and d and magnified in Fig. 4c and f. In each small unit, R'_M, R'_N, R'_O, and R'_P are radii of the local curvatures of contact lines at the two ends of the droplet. L_{MN} and L_{OP} are the lengths of the droplets on the straight and helical micro-grooved cones. $\beta \sim 25°$ is the helix angle of the helical grooves. The $F_{Laplace}$ induced in both situations scales as below:

$$F_{Laplace-Straight} \sim \gamma\left(\frac{1}{R'_N} - \frac{1}{R'_M}\right) \cdot S_{Straight}$$

$$F_{Laplace-Helical} \sim \gamma\left(\frac{1}{R'_P} + \frac{1}{R'_O}\right) \cdot S_{Helical}$$

where γ is the liquid's surface tension and $S_{Helical}$ and $S_{Helical}$ are the areas of the region enclosed by the TPCL on the helical and straight micro-grooved cones, respectively. Since $L_{OP}/\cos\beta > L_{OP} > L_{MN}$, $S_{Helical} > S_{Helical}$. In addition, with a longer droplet along the longitudinal direction of the helical micro-grooved cone, $R'_P < R'_N$, $R'_O > R'_M$, then $\left(\frac{1}{R'_P} + \frac{1}{R'_O}\right) > \left(\frac{1}{R'_P} - \frac{1}{R'_O}\right) > \left(\frac{1}{R'_N} - \frac{1}{R'_M}\right)$, we therefore have $F_{Laplace-Helical} > F_{Laplace-Straight}$ for a single groove. The overall driving force on the droplet is the integration of $F_{Laplace}$ along the entire TPCL.

In summary, the helical grooves favor the conformational transformation of droplets from the clam-shell to the barrel state, generating a different shaped TPCL and larger area enclosed by the TPCL, resulting in a larger driving force. Under similar hysteresis, the droplet shows a smaller minimal volume and higher velocity to move directionally on the helical micro-grooved cones, compared with motion on the cones with straight micro-grooves.

4.1. Fog collection experiment

To further investigate the fog collection performance of the two types of micro-grooved cones, a system integrated with cones and fast water-absorbing wood was designed. According to

a previous report, droplets accumulated at the base of an one-dimensional fog collector would impede subsequent droplet's transport, bringing adverse effects to water harvest. Therefore, fast removal of water droplets at the cone base is of great importance for efficient fog collection. To accelerate the droplet removal, we fixed the base of the cones on delignified balsa wood, being a fast water absorber. Fig. 5a and b show the scheme and real image of the cone-wood integrated fog collection system. A special note is given to the color change of balsa wood from being initially brown to being white after delignification treatment for around 6 hours (Fig. S8a†). Such a change indicates the successful removal of the greater part of lignin in the wood, which is consistent with the wood's mass change along treating time (Fig. S8d†).

Fig. 5c shows a typical sectional view of the balsa wood after 6 hour treatment, indicating a well-preserved honeycomb-like porous structure. We regulated the delignification time and probed the water absorption rate of the post-treated wood. Compared with the relatively slow water-absorption on the natural balsa wood, the delignified wood shows much more rapid water-absorbing ability (Fig. 5d, S9 and S10†). And the completely absorbing time decreases with increasing treating time. To probe the underlying reason, we checked the FT-IR spectra of the wood samples after varied delignification times. As can be seen from Fig. 5e, the initial sharp peaks at 1593 and 1505 cm^{-1} for the aromatic skeleton disappear after treatment, indicating the removal of lignin. Moreover, the peak at 3340 cm^{-1} corresponds to the characteristic O–H stretching increased with longer treating time, which reflects the increase of hydroxyl groups during lignin removal (Fig. 5e).[32–34] The abundant hydroxyl groups lead to the fast water absorption of the treated balsa wood. To be noted, although the water absorbing rate increases with prolonged treating time, the mechanical properties decrease with the delignification time. Specifically, at 6 hours of treatment, the delignified wood shows excellent mechanical properties, without structural failure under finger press. However, serious decomposition of lignocellulose (~25% weight decrease) is observed when the delignification time is increased to 10 hours. At this time, the bulk wood would easily get destroyed, making it unsuitable for use here (Fig. S8†). During fog collection, water is transported from the cone to the sample of delignified wood continuously. In this study, we investigate the water absorption properties of the wood through successive droplet additions. As shown in Fig. S11 and S12,† the delignified balsa wood absorbs a 5 μL water droplet in less than 0.13 s during 10 cycles of water droplet

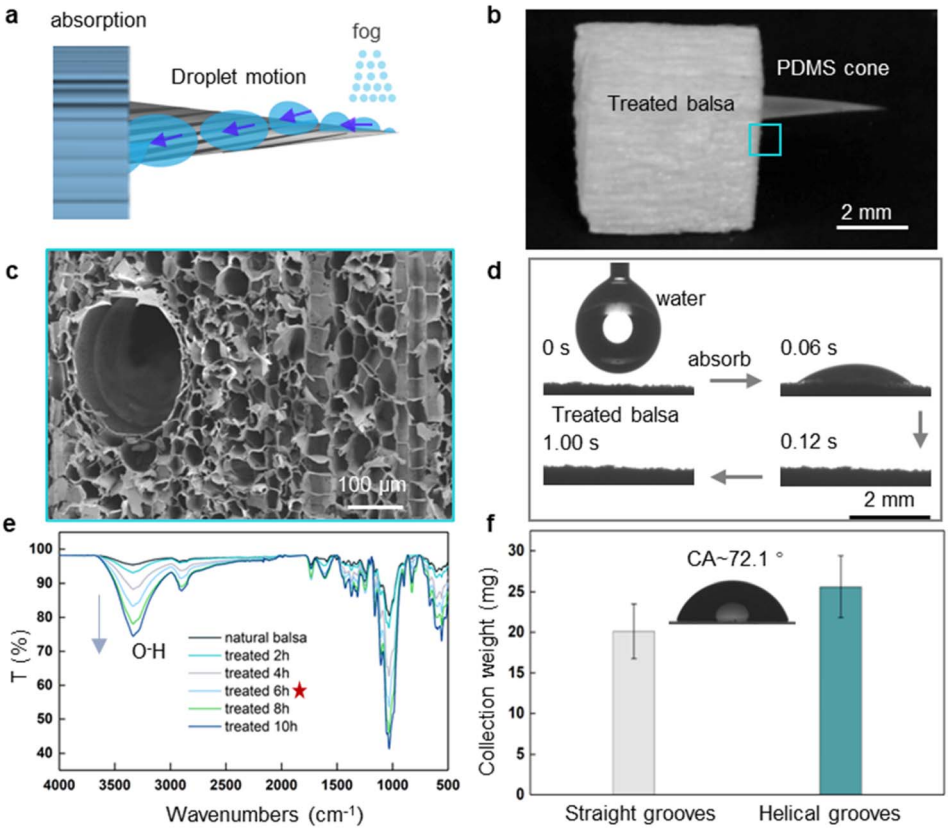

Fig. 5 Fog collection performance of a micro-grooved cone-wood system. (a) Diagram and (b) photograph of the fog collection system. The cone's base was fixed to the delignified balsa wood, which acts as a fast water absorber. (c) SEM image of the cross section of balsa wood after 6 hour delignification treatment. The honeycomb-like cell wall architecture of the native wood is well preserved. (d) Fast water absorption of the balsa wood after delignification. 5 μL water is absorbed into the wood completely in 0.12 s. (e) FT-IR spectra of the balsa wood after receiving different times of delignification treatment. With prolonged treating time, the content of hydrophilic hydroxyl groups increases. (f) Fog collection behavior of the straight/helical micro-grooved cones over a 30 min period. The system with a helical micro-grooved cone collects more water than that with a straight micro-grooved cone.

addition, indicating its efficient water absorption properties. Therefore, considering the water-absorbing rate and mechanical performance, 6 hour treatment is chosen for the following work unless otherwise specially noted.

The continuous water harvesting performance of the wood-cone integrated system was characterized using the custom-made setup at room temperature (T = 25 °C). As shown in Fig. S13,† tiny water droplets deposited on the cone move directionally from the tip to the base while coalescing into one big droplet and being absorbed by the delignified wood within 10 s. The coalesced water droplet is in clam-shell and barrel conformation on the straight and helical micro-grooved cones, respectively. Moreover, the time required for the droplet to move from the tip to the base of the straight and helical micro-grooved cones is 6 min 01 s and 3 min 51 s, respectively, indicating the faster droplet motion velocity on the helical micro-grooved cone. These results coincide well with the results shown in Fig. 2 and 3. As a result, the amount of water collected by the fog collection system with a helical micro-grooved cone is 25.6 mg, which is higher than that with a straight micro-grooved cone with 20.2 mg in the same 30 min. The results demonstrate that cones with helical micro-grooves could enhance the directional motion ability of the liquid droplet on them and hence increase the water harvesting efficiency of the system based on them.

5. Conclusion

In summary, we successfully fabricated a cone with helical micro-grooves, realizing ultrafast water transport by mimicking gradient helical micro-grooves on a natural cactus spine. To unveil the underlying mechanism, the different droplet motion behaviors on straight and helical micro-grooved cones were investigated and the corresponding Laplace force was estimated. The helical micro-groove results in barrel droplet conformation and prolonged droplet length, providing larger Laplace force. Compared with the straight micro-grooved cone, the helical micro-grooved cone shows smaller critical droplet motion volume and larger droplet motion velocity. A fog collector consists of a wood-based absorber and a micro-grooved cone is also fabricated. The fog collection efficiency of the collector with a helical micro-grooved cone (25.6 mg) is higher than that of the fog-collector with a straight micro-grooved cone (20.2 mg). This helical micro-groove design provides a new model to accelerate liquid transport, which is highly desirable in the applications of fog collection, heat radiators, microfluidic chips and cardiac pumping.

Conflicts of interest

There are no conflicts to declare.

Acknowledgements

This work was financially supported by the National Natural Science Foundation of China (22172045, 22205056, 21905076, and 21905077), the Key Science Foundation Project of Henan Province (232300421146), the China Postdoctoral Science Foundation (2021M701068), The Opening Project of the Engineering Research Center of Eco-friendly Polymeric Materials, Ministry of Education (EFP-KF2206), The Opening Project of CAS Key Laboratory of Bio-inspired Materials and Interfacial Science, Technical Institute of Physics and Chemistry (BMIS202113), and The Key Research Program of Higher Education of Henan Province (22A430003).

References

1 A. R. Parker and C. R. Lawrence, *Nature*, 2001, **414**, 33–34.
2 Y. Zheng, H. Bai, Z. Huang, X. Tian, F.-Q. Nie, Y. Zhao, J. Zhai and L. Jiang, *Nature*, 2010, **463**, 640–643.
3 J. Ju, H. Bai, Y. Zheng, T. Zhao, R. Fang and L. Jiang, *Nat. Commun.*, 2012, **3**, 1247.
4 H. Chen, T. Ran, Y. Gan, J. Zhou, Y. Zhang, L. Zhang, D. Zhang and L. Jiang, *Nat. Mater.*, 2018, **17**, 935–942.
5 J. Ju, K. Xiao, X. Yao, H. Bai and L. Jiang, *Adv. Mater.*, 2013, **25**, 5937–5942.
6 K. Zhang, H. Chen, T. Ran, L. Zhang, Y. Zhang, D. Chen, Y. Wang, Y. Guo and G. Liu, *ACS Appl. Mater. Interfaces*, 2022, **14**, 33993–34001.
7 S. Zhang, M. Chi, J. Mo, T. Liu, Y. Liu, Q. Fu, J. Wang, B. Luo, Y. Qin, S. Wang and S. Nie, *Nat. Commun.*, 2022, **13**, 4168.
8 B. Xu, Q. Wang, Q. a. Meng, M. He, C. Guo, L. Jiang and H. Liu, *Adv. Funct. Mater.*, 2019, **29**, 1900487.
9 D. Xie, Y. Sun, Y. Wu, K. Wang, G. Wang, F. Zang and G. Ding, *Adv. Mater.*, 2022, 2208645.
10 K. Li, J. Ju, Z. Xue, J. Ma, L. Feng, S. Gao and L. Jiang, *Nat. Commun.*, 2013, **4**, 2276.
11 M. Aliabadi, W. Konrad, T. Stegmaier, Y. Liu, B. Zhan, G. Wang, C. Kaya and G. Gresser, *Sep. Purif. Technol.*, 2023, **305**, 122405.
12 Y. Li, Z. Cui, G. Li, H. Bai, R. Dai, Y. Zhou, Y. Jiao, Y. Song, Y. Yang, S. Liu and M. Cao, *Adv. Funct. Mater.*, 2022, **32**, 2201035.
13 S. Wang, R. Zhou, Y. Hou, M. Wang and X. Hou, *Chin. Chem. Lett.*, 2022, **33**, 3650–3656.
14 P. S. Mahapatra, R. Ganguly, A. Ghosh, S. Chatterjee, S. Lowrey, A. D. Sommers and C. M. Megaridis, *Chem. Rev.*, 2022, **122**, 16752–16801.
15 J. Wang, S. Yi, Z. Yang, Y. Chen, L. Jiang and C.-P. Wong, *ACS Appl. Mater. Interfaces*, 2020, **12**, 21080–21087.
16 L. Xiao, G. Li, Y. Cai, Z. Cui, J. Fang, H. Cheng, Y. Zhang, T. Duan, H. Zang, H. Liu, S. Li, Z. Ni and Y. Hu, *Chem. Eng. J.*, 2020, **399**, 125139.
17 F. Bai, J. Wu, G. Gong and L. Guo, *Adv. Sci.*, 2015, **2**, 1500047.
18 D. Gurera and B. Bhushan, *J. Colloid Interface Sci.*, 2019, **551**, 26–38.
19 W. Gao, X. Feng, A. Pei, C. R. Kane, R. Tam, C. Hennessy and J. Wang, *Nano Lett.*, 2014, **14**, 305–310.
20 C. Maurel and P. Nacry, *Nat. Plants*, 2020, **6**, 744–749.
21 H. Chang, Q. Liu, J. F. Zimmerman, K. Y. Lee, Q. Jin, M. M. Peters, M. Rosnach, S. Choi, S. L. Kim and H. A. M. Ardoña, *Science*, 2022, **377**, 180–185.

22 P. P. Sengupta, A. J. Tajik, K. Chandrasekaran and B. K. Khandheria, *JACC Cardiovasc. Imaging*, 2008, **1**, 366–376.
23 L. Gao, F. Guo, N. Li, Y. Wang, Z. Guo, J. Xiong and Y. Zhao, *Adv. Eng. Mater.*, 2022, **24**, 2101753.
24 C. Li, H. Dai, C. Gao, T. Wang, Z. Dong and L. Jiang, *Proc. Natl. Acad. Sci. U. S. A.*, 2019, **116**, 12704–12709.
25 C. Yu, C. Li, C. Gao, Z. Dong, L. Wu and L. Jiang, *ACS Nano*, 2018, **12**, 5149–5157.
26 R. Mi, C. Chen, T. Keplinger, Y. Pei, S. He, D. Liu, J. Li, J. Dai, E. Hitz, B. Yang, I. Burgert and L. Hu, *Nat. Commun.*, 2020, **11**, 3836.
27 H. B. Eral, J. de Ruiter, R. de Ruiter, J. M. Oh, C. Semprebon, M. Brinkmann and F. Mugele, *Soft Matter*, 2011, **7**, 5138–5143.
28 B. Carroll, *Langmuir*, 1986, **2**, 248–250.
29 L. Lorenceau and D. Quéré, *J. Fluid Mech.*, 2004, **510**, 29–45.
30 H. Bai, X. Tian, Y. Zheng, J. Ju, Y. Zhao and L. Jiang, *Adv. Mater.*, 2010, **22**, 5521–5525.
31 B. Hu, Z. Duan, B. Xu, K. Zhang, Z. Tang, C. Lu, M. He, L. Jiang and H. Liu, *J. Am. Chem. Soc.*, 2020, **142**, 6111–6116.
32 J. Song, C. Chen, Z. Yang, Y. Kuang, T. Li, Y. Li, H. Huang, I. Kierzewski, B. Liu, S. He, T. Gao, S. U. Yuruker, A. Gong, B. Yang and L. Hu, *ACS Nano*, 2018, **12**, 140–147.
33 T. Yang, J. Cao and E. Ma, *Ind. Crops Prod.*, 2019, **135**, 91–98.
34 V. Emmanuel, B. Odile and R. Celine, *Spectrochim. Acta, Part A*, 2015, **136**, 1255–1259.